ACS Sustainable Resource Management

pubs.acs.org/acssrm

Open Access

This article is licensed under CC-BY 4.0

Article

High-Throughput Graphite Recovery from Battery Anode Scrap, Impacts of Using In-Line Near-Infrared Processing on Material Integrity

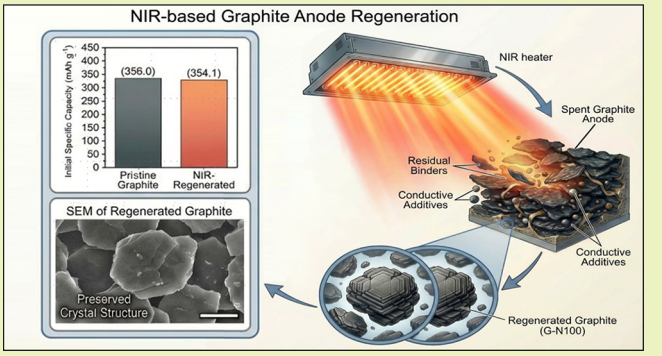
Wafaa Al-Shatty, Oriyomi O. Ogunbanjo, Harrison Fell, Oli Fryatt, Pierrot S. Attidekou, Gavin Harper, Paul A. Anderson, Davide Deganello, and Jenny Baker*

Cite This: *ACS Sustain. Resour. Manag.* 2026, 3, 2751−2765

Read Online

ACCESS | Metrics & More | Article Recommendations | Supporting Information

ABSTRACT: Graphite, the predominant anode material in lithium-ion batteries (LIBs), accounts for a substantial share of both battery mass and cost. However, the recycling of graphite anodes remains energetically and technically challenging since residual binders and electrically conductive additives hinder effective material recovery and can degrade reusability and electrochemical performance. This work outlines a new thermal approach to regenerate graphite anodes based on near-infrared (NIR) irradiation, which enables rapid binder deactivation, and benchmarks its performance against conventional furnace heat treatment. Model graphite anode composites comprising graphite, carbon black, and representative aqueous binders (carboxymethyl cellulose and styrene−butadiene rubber) were prepared and subjected to a range of furnace and NIR exposure conditions. Our results demonstrate that furnace treatment at 450–470 °C for 60–120 min and NIR irradiation at 100% intensity for only 15.6 s at a line speed of 2 m/minute can effectively deactivate binders without compromising the graphite crystal structure. In terms of electrochemical performance, the NIR-regenerated graphite (G-N100) delivered an initial specific capacity of 354.1 mAh g^{-1} at 10 mA g^{-1} and retained 99.9% of its capacity after 20 cycles; this represents a specific capacity that is 99.4% of pristine graphite (356.0 mAh g^{-1}) under the same conditions. In contrast, furnace-regenerated samples (G-470 and G-450) exhibited higher specific capacities of 374.7 and 373.7 mAh g^{-1} at 10 mA g^{-1}, slightly exceeding that of pristine graphite. This work demonstrates that NIR irradiation can provide a selective, ultrafast thermal route to decompose binder additives while also preserving the graphite structure and electrochemical performance with greenhouse gas emissions of 0.4 $kgCO_{2e}$/kg compared with between 1.4 and 9 $kgCO_{2e}$/kg for virgin anode grade graphite.



KEYWORDS: *graphite recovery, battery anode recycling, near infra-red heating, greenhouse gas emissions, binder removal*

1. INTRODUCTION

The demand for LIBs has increased dramatically in recent years, driven by their widespread adoption at a variety of scales, from portable electronics (~1–9 Wh), electric vehicles (EVs) (100–3500 Wh), to renewable energy storage systems (presently ≤194 MWh).[1−3] In addition to the scarcity of many of the materials required for present-day LIB production, the recent increase in LIB production volume has led to environmental concerns regarding the disposal of spent batteries, which have lifespans of only 3–10 years.[4,5] There is a clear and urgent need to recover materials from spent LIBs, in particular lithium, cobalt, nickel, manganese, and graphite, to mitigate resource scarcity and pollution.[6] Graphite, as the predominant anode material in LIBs, constitutes 15–21% of a typical battery's mass and 10–15% of its total cost, making it a critical component for sustainable battery ecosystems.[7,8] The global distribution of graphite is uneven, with Chinese production accounting for around three-quarters of the world's supply[9] and it is considered a critical material by the EU and the UK.[10−12] Recycling graphite has thus become essential for environmental preservation and sustainable resource development, yet it has often been overlooked due to its perceived low added value compared to the reclamation of high-value transition metals from cathode materials.[13] There is a clear market for recovering materials

Received: April 15, 2026
Revised: July 16, 2026
Accepted: July 20, 2026
Published: August 12, 2026



ACS Publications

© 2026 The Authors. Published by American Chemical Society

Downloaded from pubs.acs.org/asmcd/article-pdf/3/8/2751/6650751 6/rm-2026-00237h.pdf by UNIV OF BATH user on 29 October 2026

from end of life batteries, in addition there are significant material losses during battery production, both as unavoidable yield losses and losses associated with production scrap which are reported to be over 10% in mature production lines and can be significantly higher in new production lines.[14] With EV battery lifetime exceeding 10 years this material recovery route will be significant whilst battery production is ramping up and where materials can be directly collected and recycled within the same facility.

To recover graphite from LIBs, the anode must be separated from other battery components, delaminated from a metal current collector, and then any additives removed.[15] Typical additives include binders to aid slurry adhesion and conductive additives. The removal of such additives is essential for the effective recovery of high-quality graphite. For reuse of the material, its recovery must be achieved with a high yield, low energy cost, and minimal effect on the structure (and subsequently the electrochemical performance).

Binder removal is a critical step in graphite recovery, as residual binders can contaminate recycled materials, reduce electrochemical performance, and complicate impurity separation.[16] Various techniques have been explored in the literature, each with distinct pros and cons. Solvent extraction, for instance, uses highly polar organic solvents such as *N*-methyl-2-pyrrolidone (NMP), dimethyl formamide, ionic liquids (e.g., $[BMIm][BF_4]$), and molten salts such as $AlCl_3$–NaCl, to dissolve binders,[16] offering high selectivity and minimal damage to graphite structure, as demonstrated by Zhang et al.[17] who achieved over 95% binder removal efficiency. However, this process generates toxic waste and requires extensive wastewater treatment, increasing environmental and operational costs.[18] Mechanical methods, such as ball milling or ultrasonic treatment, physically dislodge binders without chemicals, providing a low-cost, eco-friendly option with studies by Yu et al.[19] reporting effective removal in spent anodes; yet, they can introduce micro-defects or contamination, reducing graphite quality.[20] Thermal treatments, including pyrolysis and roasting, decompose binders at elevated temperatures (300–700 °C), enabling scalable processing as shown in works by Lombardo et al.[21] with up to 99% removal rates. However, this approach often requires extremely high temperatures to decompose binder and reconstruct the graphite crystal structure, leading to substantial energy consumption and costs that contradict green recycling principles, limit the economic value of recycled products, and diminish interest in graphite recycling.[2,4] Microwave-assisted delamination has also been explored, using a microwave-assisted carbothermic reduction, which recovered (10–20 wt %) from mixed LCO + NCM black mass. In this process, the presence of carbon aids the process as both a microwave susceptor and reducing agent mediating the carbothermic reduction of mixed oxides.[22]

Recent focus has been placed on binder removal from various anode battery materials through thermal decomposition to improve the quality of the recycled product. Thermal decomposition aims to repair graphite structures through carbon coating or high-temperature treatment. In a study conducted by Yu et al.,[23] experiments were performed with graphitization temperatures ranging from 2400 to 2800 °C. They found that calcination at 2800 °C for 6 h was the optimal treatment for reducing internal stress and achieving a high degree of graphitization, however, a notable drawback is significant energy consumption.

Thermal oxidation has proven to be highly effective for binder deactivation and facilitating material separation. Under high-temperature conditions (typically above 800 °C), the oxidative decomposition of binders enables the separation of active materials from aluminum and copper foils. Several studies have investigated specific conditions for implementing high-temperature processing.[24,25] However, research is still required to develop scalable methods suitable for applications in the battery and electronics industries.

Given these challenges in conventional thermal heat treatment methods, alternative heating methods like NIR are being considered.[26] NIR techniques have been used in areas such as polymer degradation,[27] curing of coatings,[28] food processing, and material sorting, where NIR radiation (wavelengths 0.78–2.5 μm) provides rapid, selective heating through molecular vibrations.[29,30] Although NIR has not yet been deployed in published battery reclamation studies, its prospects in graphite recovery lie in opportunities for rapid processing, as NIR can enable targeted binder decomposition enabling inline processing with possibility of preserving graphite integrity.[31] This work considers the recovery of graphite in the case of manufacturing scrap, which has been rejected ahead of charge–discharge cycling; as such, the recycling of graphite where an SEI layer has formed is not considered in this work. To assess how effectively this thermal recovery method can separate active materials from the graphite slurry, we investigated the efficiency of a novel NIR method and compared its performance to the conventional furnace treatment separation methods. The active materials to be separated from copper foil included conductive carbon black (CB) and organic binders. We discuss the characteristics of the thermal treatment, including the decomposition temperature of the binder, carbon black, and graphite, which significantly influence the material recovery and highlight the challenges within the suggested process. Next, the heat treatment temperature, time (conventional furnace), intensity, and radiation exposure (NIR treatment) are examined in detail to study how different thermal treatments influence the physical properties, structure, and morphology of graphite, with subsequent electrochemical characterization of the recovered materials in battery cells.

Our results demonstrate that furnace treatment and NIR irradiation can effectively deactivate binders without compromising the graphite crystal structure. In terms of electrochemical performance, the NIR-regenerated graphite (G-N100) delivered an initial specific capacity of 354.1 mAh g^{-1} at 10 mA g^{-1} and retained 99.9% of its capacity after 20 cycles; this represents a specific capacity that is 99.4% of pristine graphite (356.0 mA h g^{-1}) under the same conditions.

2. EXPERIMENTAL SECTION

2.1. Materials

Pristine spherical natural graphite (PG-907154), polyvinylidene fluoride (PVDF-24937-79-9), 1-methyl-2-pyrrolidone (NMP-872-50-4), carboxymethyl cellulose (CMC-419338), and vinylene carbonate electrolyte additives (VC-872-36-6) were purchased from Sigma-Aldrich. Styrene-butadiene rubber (SBR-9003-55-8) and copper foil were from MTI Corporation, while carbon black was purchased from Imerys. The electrolyte consisted of 1 M LiPF6 in EC:EMC = 30:70 wt % purchased from Solvionic. The Celgard CR2032 and lithium metal were provided by Xiamen Tob New Energy Technology Corporation Limited, Xiamen, China. All chemicals were of analytical grade and used

Downloaded from pubs.acs.org/asmcd/article-pdf/3/8/2751/6650751 6/rm-2026-00237h.pdf by UNIV OF BATH user on 29 October 2026

https://doi.org/10.1021/acssusresmgt.6c00237
ACS Sustain. Resour. Manag. 2026, 3, 2751−2765

as received without further purification. However, SBR was left to dry at room temperature for 18 h to be characterized by Fourier transform infrared spectroscopy (FTIR) and thermogravimetric analysis (TGA).

2.2. Preparation of a Solid Graphite Anode Composite

To generate enough graphite-based anode powder representative of production-scrap-equivalent material for recycling experiments, a solid anode composite was prepared using a slurry-inspired formulation route. For the model samples, a binder of CMC-SBR was used to be applicable with the latest industry standard, and a high binder composition was chosen in order to represent the worst case for binder removal quantities. Although slurry-based mixing was initially employed to ensure homogeneous dispersion of the components, the intended final material was a dry, free-flowing solid rather than a wet slurry. A demonstration of this method can be seen online.[32]

CMC (0.24 g) was dissolved in deionized water (2 wt %) and stirred at 1500 rpm (using a magnetic stirrer) for 48 h, forming a clear homogeneous solution. After time passed, CB (0.24 g) was added to the CMC solution and mixed for 5 min using a mechanical mixer (AMD20). Graphite anode powder (11.2 g) was added and mixed (mechanical mixer) for 5 min, and then 6 g of deionized water was added.

The mixture was left for 18 h to settle down before adding SBR (0.48 g) and mixed for 5 min. The material was then left in a fume hood for 18 h at laboratory temperature to allow complete evaporation of water, yielding a dry solid composite used in a two-stage experimental approach. In stage I, the dried composite powder was hand-ground using an agate mortar and pestle (Sigma-Aldrich) and sieved to obtain a particle size of <125 μm, and then used directly in recycling experiments to represent production-scrap-equivalent material. In stage II, the same recipe was coated onto a copper current collector foil and subjected to the same treatment to assess the influence of the current collector.

2.3. Thermal Treatment Methods

After mechanical removal from the copper foil, approximately 0.40 g of the dried slurry powder (particle size <125 μm) was placed in an alumina crucible and subjected to two types of thermal treatments. In the first method, samples were heated in a Carbolite CWF 1200 box furnace: The powder was ramped from room temperature at 10 °C min^{-1} to the target temperature, held for the designated time, and then cooled to ambient temperature. Furnace treatments included heating at 350 °C (for 15, 30, or 60 min), at 450 °C (for 15, 30, 60, or 120 min), and at 470 °C (for 60 min).

In the second method, samples in the alumina crucible were exposed to NIR irradiation: The NIR lamp intensity was set to 60%, 80%, or 100% of maximum output where 100% output corresponds to a lamp power density of 1200 kW/m^2, and samples were irradiated for 7.8 or 15.6 s (residence time under the lamp). A schematic including lamp spectra and a photograph of the NIR heating set up are given in the Supporting Information Figures S1 and S2, respectively.[33]

During NIR treatment, the material temperature is difficult to measure due to the rapid and transient nature of exposure. The NIR itself interferes with nickel-based thermocouples preferentially absorbing NIR and therefore measuring a temperature reading that does not reflect that of the material being processed. In addition, the NIR itself can interfere with optical non-contact measurements. The specific temperature reached by the material depends on several factors, including optical absorption, emissivity, residual solvent, thermal mass, substrate cooling, and heat losses. NIR itself interferes with no contact measurements. For this reason, the treatment is more reproducibly described by the controlled irradiation parameters: NIR power, residence time, and lamp power density.

The potential peak temperature can be modeled; however, this is subject to significant assumptions, which are included in the Supporting Information; Figure S1c gives a predicted temperature of material 460 °C, but this should be treated with caution. Further work is being undertaken to refine and validate this model.

Upon identifying the conditions required for effective binder deactivation, 2 g of material from both stage I and stage II samples was subjected to these conditions. Figure 1a presents a schematic overview of the graphite dry-slurry processing route from stage I and subsequent thermal treatment.

2.4. Analytical Instruments and Methods

To obtain the decomposition temperature of the sample, TGA was performed using Netzsch STA 441 F1 Jupiter + Mass Spectrometer at a 10 °C/min ramp rate (atmosphere, 100 mL/min) in an alumina crucible. The tested powder sample (10 ± 2 mg) was heated from 25 to 900 °C, with data presented showing an average of three repeats. FTIR was used to characterize the organic binders at wavelengths 550 to 4000 cm^{-1} (32 scans); however, organic binders were below the detection limit of the FTIR when incorporated into the dried composite powder. Surface morphologies were analyzed using a scanning electron microscope (SEM, JEOL F2900, and 2900 FEG-SEM) equipped with a tungsten filament and coupled with an energy-dispersive spectrometer (EDS). The structure of each graphite sample was investigated with a Bruker D8 Avance X-ray diffractometer in Bragg–Brentano θ/2θ geometry (40 kV, 30 mA) with Cu Ka radiation (λ = 1.5406) operated in the 2θ range from 5° to 70° with a scan speed of 1 s/step and a step size of 0.05. A flat reflection sample holder was used with samples packed onto a zero-background silicon substrate. Preferred orientation effects are expected in this geometry for graphite powder and affect both peak intensities and the relative intensities of the (001) reflections; no internal standard was applied for peak position correction, since the objective was comparative structural characterization across the sample series. Raman microscopy (Renishaw inVia and Leica PL Fluotar) was performed with a 532 nm laser and a 20× working distance objective lens. Data was acquired for all samples across the range $1000 \leq \tilde{\nu} \leq 3000\ cm^{-1}$ at 10% laser power for a total of 10 min and repeated at eight sites across each sample. Peak analysis was performed with OriginPro 2025b. Nitrogen sorption isotherms were produced using 3Flex (Micromeritics). The specific surface areas and pore size distributions were calculated using Brunauer–Emmett–Teller (BET) and Barrett–Joyner–Halenda models, respectively. The copper current collector was removed prior to any characterization powders (SEM/XRD/TGA/Raman/surface area) of powders.

2.5. Electrochemical Testing

To analyze the electrochemical performance of the graphite samples, a slurry of the sample was made by mixing graphite active material (AM), CB, and PVDF into NMP (55 wt %), at a ratio of 92:6:2 of AM:PVDF:CB by mass. A PVDF system was chosen to ensure the highest-performing cells possible without masking poor graphite performance with manufacturing defects.

The slurry was coated uniformly on a 9 μm copper foil (MTI Corporation) using a doctor blade set to a thickness of 200 μm. The coated foil was first dried on a hot plate at 80 °C and then transferred to a vacuum oven and held at 100 °C for 24 h. The resulting dried electrode was subsequently calendared at 70 °C to attain a porosity of 40–45%, followed by an additional 24 h of vacuum drying. A 2032-coin cell was assembled in an argon-filled glovebox in which the concentrations of O_2 and H_2O were less than 0.1 ppm. Anode disks (15 mm diameter, 6–10 mg active material loading) were punched from the coated electrodes and assembled into half-cells using lithium metal as the counter electrode (PI-KEM; 15.6 mm diameter, 0.25 mm thickness). Glass microfiber (Whatman GC/C, 1.2 mm thick, 55 mm diameter) was used as the separator and 80 μL of 1 M lithium hexafluorophosphate ($LiPF_6$) in ethylene carbonate/ethyl methyl carbonate (EC/EMC, 30:70 wt %) supplemented with 2 wt % vinylene carbonate additives as electrolyte. The coin cells were rested for 12 h to equilibrate before being tested on a battery cycler. Electrochemical studies were carried out using a BioLogic SP-50 cell tester. Galvanostatic charge–discharge testing was carried out at a voltage window of 0.005–1.5 V vs Li/Li^+ and charging currents of 10 and 40 mA g^{-1}. Cycling voltammetry

Downloaded from pubs.acs.org/asmcd/article-pdf/3/8/2751/6650751 6/rm-2026-00237h.pdf by UNIV OF BATH user on 29 October 2026

https://doi.org/10.1021/acssusresmgt.6c00237
ACS Sustain. Resour. Manag. 2026, 3, 2751−2765

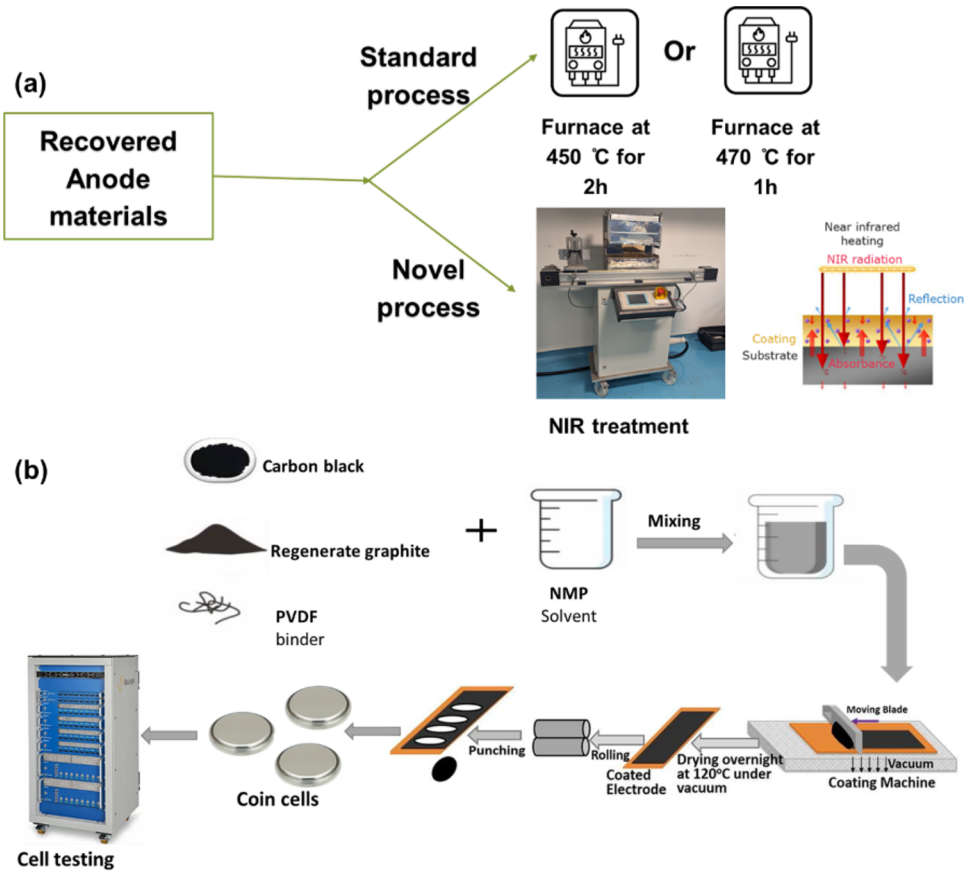


Figure 1. Schematic diagram of (a) thermal treatments of recovered anode materials and (b) coin cell fabrication and testing.

(CV) testing was conducted at sweep rates of 0.1, 0.2, 0.3, and 0.5 mV/s in the range from 0.005 V to 1.5 V. Electrochemical impedance spectroscopy (EIS) tests were recorded in the frequency range of 1 MHz to 0.01 Hz using a perturbation voltage amplitude, $V_a = 2$ mV RMS, at 10 points per decade at 0.2, 0.1, and 0.07 V. All cell data were collected in triplicate. Figure 1b presents a schematic overview of the assembly of coin cells and the corresponding electrochemical evaluation workflow.

3. RESULTS AND DISCUSSION

3.1. Thermal Treatment

This work considers the recovery of graphite in the case of manufacturing scrap, which has been rejected ahead of charge–discharge cycling; as such, the recycling of graphite where an SEI layer has formed is not considered in this work. The yields of graphite recovered after different thermal and NIR treatments are summarized in Table S2. For furnace-treated samples at 450 °C, mass loss increased with longer processing times: 15 and 30 min treatments resulted in minimal yield reduction (2.89% and 3.33%, respectively), while 60 min led to slightly higher mass loss (5.45%). Extended heating for 120 min caused more significant losses, with yields ranging from 8.88% to 13.35% (mean ± SD: 11.33 ± 1.88%), reflecting progressive binder decomposition and partial carbon volatilization. Furnace treatment at 470 °C for 60 min showed a similar trend, with yields between 10.25% and 13.40% (11.59 ± 1.63%), indicating slightly accelerated decomposition at higher temperature. NIR-assisted regeneration also effectively decomposed binder additives while preserving the graphite structure, with yields for the 60–100% power, 15.6 s treatments ranging from 7.37% to 12.32% (10.54 ± 1.72%). Overall, these results demonstrate that both thermal and NIR treatments achieve reproducible graphite recovery, with NIR processing providing an ultra-fast alternative that maintains comparable yields to conventional furnace approaches.

The thermal behavior of graphite and composite anode material was evaluated by TGA in air at heating rates of 5 and 10 °C min^{-1}. Pristine graphite showed negligible mass loss below ~639 °C (Figure 2a), confirming the absence of volatile species and indicating high structural stability.[34,35] A single, well-defined oxidation step was observed at both heating rates, characteristic of homogeneous and highly crystalline graphite. The maximum oxidation temperatures (T_max) were 812 °C (5 °C min^{-1}) and 795 °C (10 °C min^{-1}). The slight shift to a lower temperature at a higher heating rate is attributed to kinetic and heat-transfer limitations, confirmed in Figure 2b where with a 3 h hold all the graphite decomposes at just 690 °C. The narrow DTG peaks in Figure 2a further confirm high purity and minimal amorphous carbon content.

The presence of binders and conductive additives significantly altered the degradation behavior. SBR decomposed predominantly between 400 and 500 °C (Figure 2c), markedly reducing the thermal stability of the composite. In Graphite–SBR (G-SBR) systems (Figure 2c,d), degradation occurred earlier than in pure graphite, suggesting that the presence of SBR facilitates graphite decomposition. The presence of carbon black (Figure S9) broadened the oxidation profile and shifted peak positions, likely due to its high surface area and influence

https://doi.org/10.1021/acssusresmgt.6c00237
ACS Sustain. Resour. Manag. 2026, 3, 2751−2765

Downloaded from pubs.acs.org/asmcd/article-pdf/3/8/2751/6650751 6/rm-2026-00237h.pdf by UNIV OF BATH user on 29 October 2026

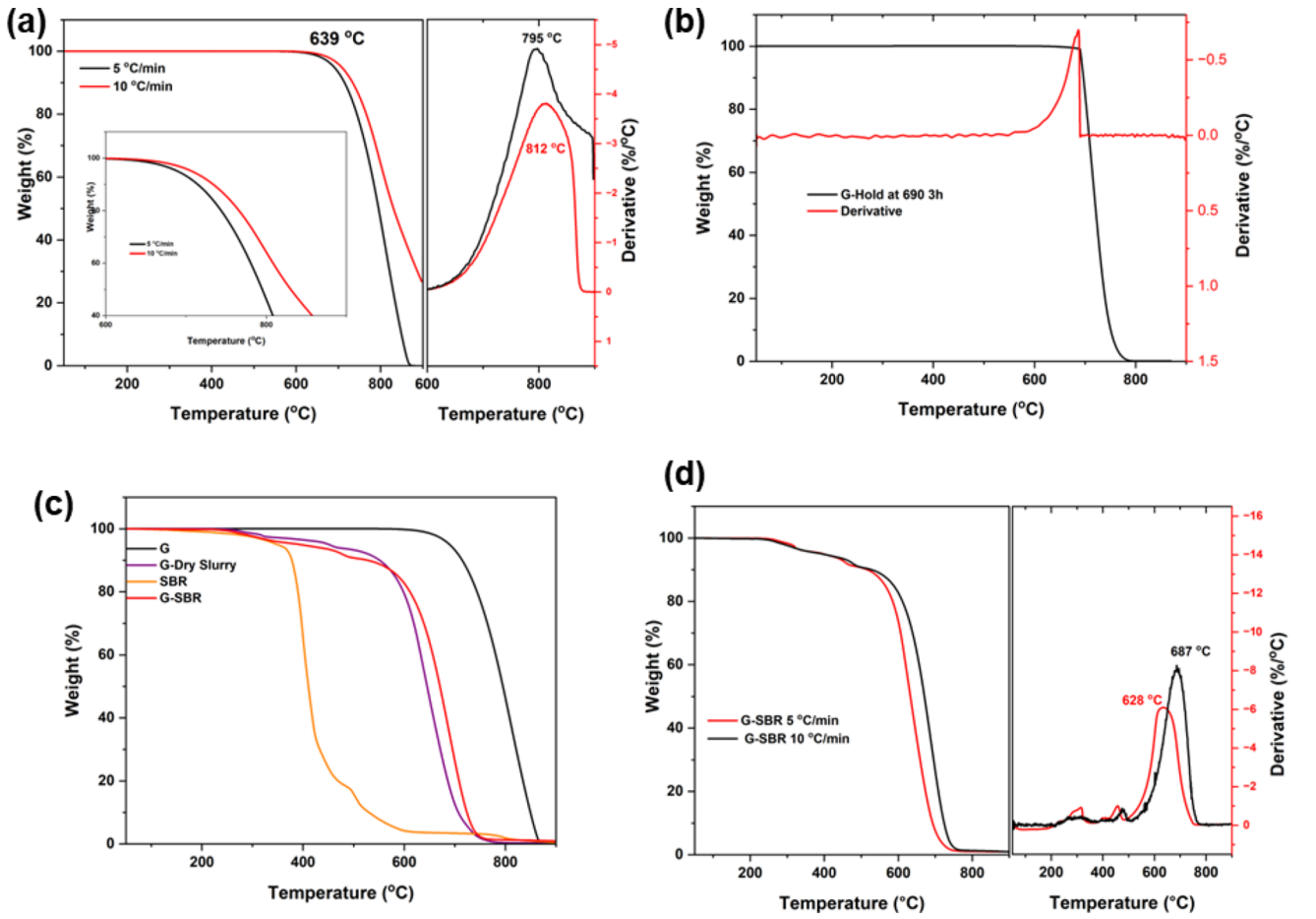


Figure 2. TGA/DTG profiles of (a) pristine graphite at 5 and 10 °C min^{-1}. (b) TGA/DTG curves of G-Hold (690 °C, 3 h) showing negligible low-temperature mass loss and a single major oxidation event associated with graphite combustion, confirming effective removal of organic residues during the holding treatment. (c) TGA profiles of graphite (G), dry slurry-derived graphite (G-Dry Slurry), SBR, and graphite containing SBR (G-SBR). The results reveal distinct thermal degradation of the SBR binder at lower temperatures and graphite oxidation at higher temperatures, enabling identification of the temperature window for selective binder removal. (d) Pure SBR at 5 and 10 °C min^{-1} in air. All curves are an average of two repeats.

on heat and oxygen transport. Increasing the heating rate shifted the apparent oxidation region to higher temperatures, consistent with thermal lag effects.[36] Complete datasets are provided in the Supporting Information (Figures S3–S7).

For the dried graphite slurry (G- slurry), a distinct mass loss was observed between ~250 and 450 °C (Figure 3a), corresponding to the decomposition of CMC and SBR binders. This feature was absent in G-450, G-470, and G-N100, confirming effective binder removal after thermal or NIR treatment. All samples exhibited the main graphite oxidation between ~600 and 750 °C; however, treated samples showed slightly higher onset temperatures and sharper DTG peaks, indicating reduced defect density and improved structural ordering.

Notably, G-N100 displayed oxidation behavior comparable to G-450 and G-470, demonstrating that 100% NIR irradiation for 15.6 s (equivalent to a line speed of 2 m/min with a 40 cm emitter) achieves similar binder removal and structural stabilization to conventional heating at 450–470 °C. Residual mass remained below 2% for all treated samples. Individual TGA plots for each treatment are included in the supporting document, Figures S11–S13.

TGA of pure SBR identified the thermal conditions required for complete removal, with full decomposition at 470 °C for 60 min and substantial removal at 450 °C for 120 min (Figure 3b). Near-complete elimination was also achieved by 100% NIR irradiation for 15.6 s (Figure 3c). These results demonstrate that optimized thermal or NIR processing enables selective binder decomposition while preserving graphite structure, providing an energy-efficient route for electrode purification and recycling. Table 1 summarizes the nomenclature of all samples investigated in this work, including their corresponding processing conditions and material characteristics.

3.2. Surface Morphology Analysis Using SEM and the N_2 Adsorption

Figure 4 presents the morphologies of pristine graphite powder (G-pristine), G-slurry, and the regenerated graphite subjected to three post-treatment conditions: furnace annealing at 450 °C for 2 h (G-450) and 470 °C for 1 h (G-470), and NIR irradiation at 100% intensity in two runs of 7.8 s each (G-N100). The SEM image of the pristine graphite (Figure 4a) reveals the plate-like flake morphology of natural graphite. Post-heat treatment at 450 and 470 °C, the flake morphology of the graphite is largely retained (Figures 4d,e); however, irregular particle-like features are evident on the surface for these samples. The NIR-treated sample (Figure 4e) likewise

Downloaded from pubs.acs.org/asmcd/article-pdf/3/8/2751/6650751 6/rm-2026-00237h.pdf by UNIV OF BATH user on 29 October 2026

https://doi.org/10.1021/acssusresmgt.6c00237
ACS Sustain. Resour. Manag. 2026, 3, 2751−2765

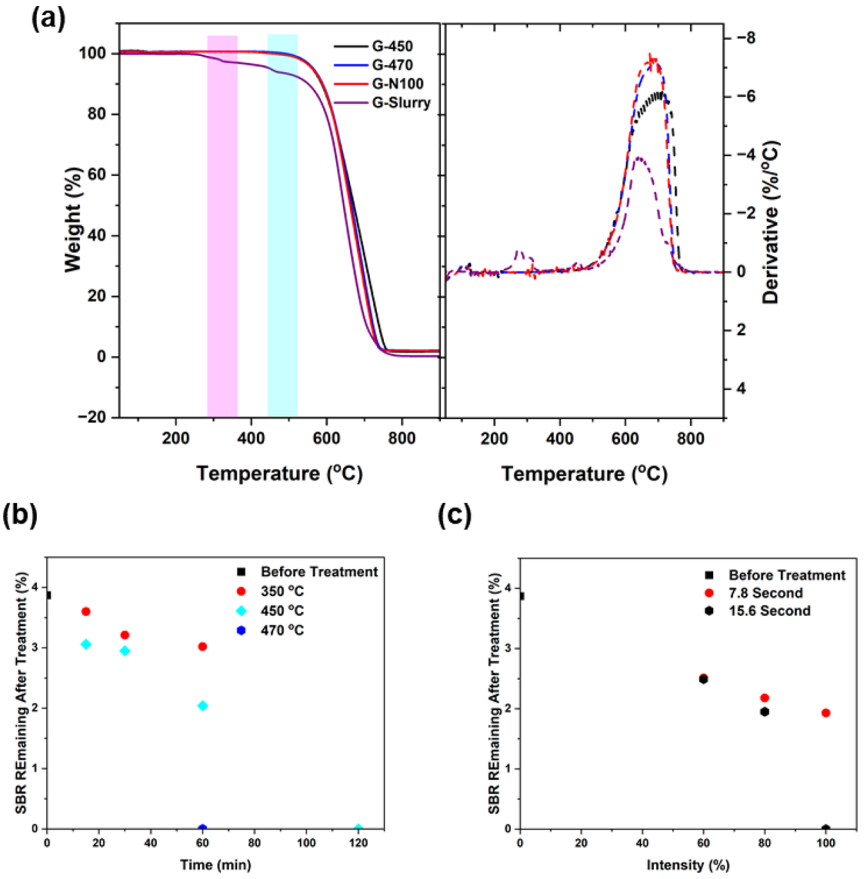


Figure 3. TGA curve of the graphite slurry treated at the optimized furnace and NIR conditions (a), plot showing the percentage of SBR before and after furnace and NIR treatment under all the testing conditions (b) and (c). The pink highlighted the area representing the decomposition temperature of the CMC binder, and the blue area represents the decomposition temperature of the SBR binder.

Table 1. List of Sample Names

Sample name in paper	Refers to
G-pristine	Pristine graphite (PG-907154)
G-slurry	Dried graphite slurry powder
G-470	Dried graphite slurry powder that was treated at a conventional furnace at 470° C for 1 h
G-450	Dried graphite slurry powder that was treated at a conventional furnace at 450° C for 2 h
G-N100	Dried graphite slurry powder that was treated at NIR 100 % for 15.6 s

shows no obvious structural damage, indicating that the brief, high-intensity NIR exposure did not compromise the graphite flakes. In all thermally treated samples, small dark spots are visible on the surface, consistent with residual carbon black that remained undecomposed under the applied heating conditions.

The N_2 adsorption–desorption isotherm curves and the BET-specific surface area (SSA) values of the investigated graphite samples are shown in Figure 4f. The G-pristine exhibited an SSA of 3.11 $m^2 g^{-1}$, which decreased to 2.79 $m^2 g^{-1}$ for G-slurry. This reduction is consistent with literature reports[37] showing that polymeric binder addition can mask or occlude graphite surface features, leading to apparent SSA reduction due to pore blockage or coverage by additives. The CB has an SSA of ∼62.5 $m^2 g^{-1}$, in line with values reported for commonly used carbon blacks such as Super P (≈50–80 $m^2 g^{-1}$) that contribute significantly to the electrode surface area despite their low mass fraction. After thermal treatment, the SSA of the increased (Figure 4f), indicating effective decomposition and removal of binder components, revealing previously covered surfaces, similar observations have been reported in literature.[38]

The theoretical BET SSA for the graphite + carbon black composite (based on mass-weighted contributions) is ∼4.7 $m^2 g^{-1}$. The experimentally measured values after thermal treatment approach are lower than this, implying that while some CB has decomposed in the thermal treatment, a small fraction of CB remains, as observed in the SEM images (Figure 4).

Importantly, none of the treated samples exceed the theoretical composite SSA, indicating that thermal treatments did not generate substantial structural damage; similar conclusions are drawn in studies of graphite treated under controlled thermal conditions, where the surface area remains near theoretical predictions when structural integrity is preserved.[39,40]

3.3. Structural Analysis

Powder X-ray diffraction (PXRD) patterns G-pristine, G-slurry, and G-470, G-450, and G-N100 were collected (Figure 5a,b).

Downloaded from pubs.acs.org/asmcd/article-pdf/3/8/2751/6650751 6/rm-2026-00237h.pdf by UNIV OF BATH user on 29 October 2026

https://doi.org/10.1021/acssusresmgt.6c00237
ACS Sustain. Resour. Manag. 2026, 3, 2751−2765

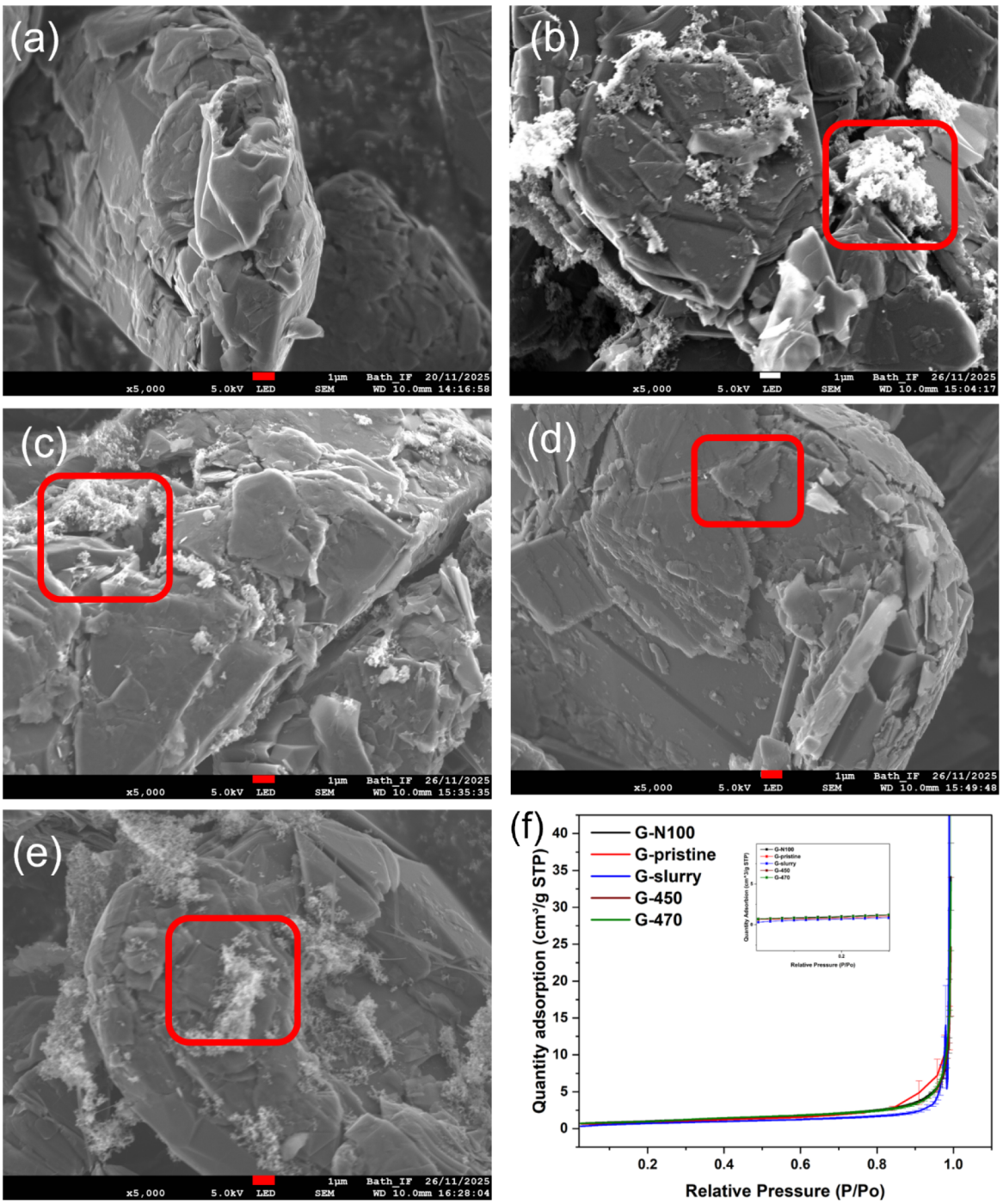


Figure 4. SEM images of powder–pristine (a), G-slurry (b), G-450 (c) G-470 (d), and G-N100 (e), with red rectangles highlighting the areas of CB. (f) N_2 adsorption–desorption isotherm curves for all samples–with inset relative pressure 0–0.3.

Each of the patterns appears as characteristic of crystalline graphite, with the sharp reflection at ∼26° corresponding to the interlayer spacing (the (002) reflection). The patterns show crystalline materials with sharp diffraction peaks. Database matching identified rhombohedral (R-3m) and hexagonal ($P6_3mc$) graphite phases, with weak reflections near $2\theta \approx 24°$ and 54° possibly due to reduced graphene oxide. As shown in Figure 5b, G-slurry showed a slight shift in peak position to higher 2θ compared to G-pristine. Upon thermal treatment, the peaks for G-470, G-450, and G-N100 shift toward lower 2θ values, approaching the pristine graphite peak. Similarly, the interplanar spacing $d(002)$ (calculated based on Bragg's equation:[24] $2d \sin\theta = n\lambda$) for G-470, G-450, and G-N100 was evaluated to be 0.332, 0.333, and 0.333 nm, respectively, unchanged compared with the G-slurry (0.3320 nm). The d_{002} values we report for the treated samples (0.332–0.333 nm) are marginally below the theoretical value for ideal graphite, the most likely dominant explanation is a systematic measurement artifact arising from the strong preferred orientation of graphite powder in a flat Bragg–Brentano sample holder.

https://doi.org/10.1021/acssusresmgt.6c00237
ACS Sustain. Resour. Manag. 2026, 3, 2751−2765

Downloaded from pubs.acs.org/asmcd/article-pdf/3/8/2751/6650751 6/rm-2026-00237h.pdf by UNIV OF BATH user on 29 October 2026

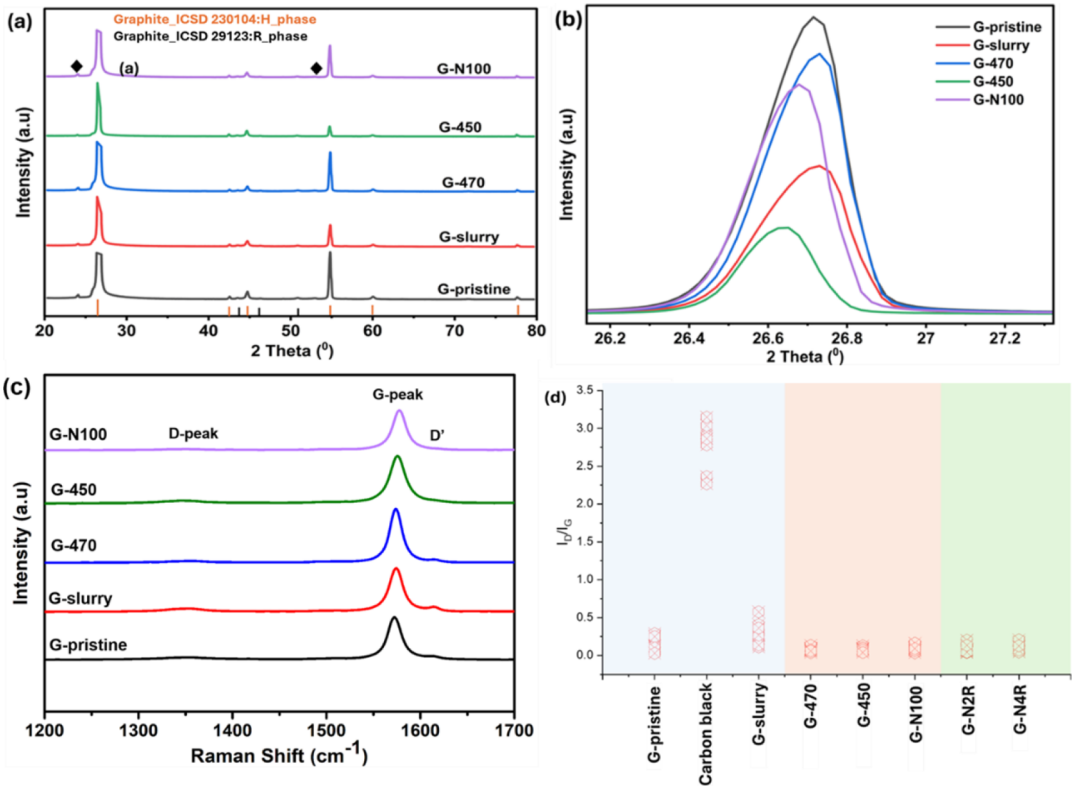


Figure 5. XRD patterns (representative plots) of (a) G-pristine, G-slurry, G-470, G-450, and G-N100. (b) Local enlargement of (a) at 2θ of 26°–27° (c). Raman spectra presented is an average of eight positions (d), and a plot showing I_D/I_G ratio for the six samples.

Natural graphite flakes are highly anisotropic and align with their basal planes parallel to the flat sample surface during loading. In Bragg–Brentano θ/2θ geometry, this preferred *c*-axis orientation causes the (002) peak to shift systematically toward higher 2θ relative to its position in a randomly oriented powder. By Bragg's law, a higher 2θ position produces a lower calculated *d*-spacing. An artifact can shift the apparent d_{002} below the theoretical value even for a well-crystallized sample. The difference between the interplanar spacings of disordered carbon and ideal graphite d_{002} is only 0.003 nm, making absolute peak position measurement prone to errors from sample height variation, instrument misalignment, and preferred orientation, all of which affect the calculated *d*-spacing.

A secondary contributing factor is residual compressive microstrain along the *c*-axis. If a crystallite is under compressive stress, the *d*-spacings contract, shifting the diffraction peak toward higher 2θ and producing a smaller apparent *d*-spacing by Bragg's law. Thermal and NIR treatment can impart transient compressive strains at graphite particle surfaces through differential thermal contraction on cooling. Finally, the presence of a rhombohedral graphite polytype (confirmed by our database matching) introduces a slight deviation from the single-phase hexagonal reference, shifting the weighted-average d_{002} marginally from 0.335 nm.

While literature suggests that thermal treatment reorganizes the carbon atoms in the graphite slurry from a relatively disordered arrangement toward a more ordered crystalline structure and our data supports this trend, it is not possible to conclude this with certainty due to limitations in the XRD experimental setup.[41,42] Peak intensity reflects the number of atoms capable of X-ray scattering and is related to crystallinity.[43] G-pristine exhibited higher peak intensity, indicating a higher degree of graphitic ordering, whereas G-slurry and the thermally treated samples showed lower intensities, consistent with the presence of binders and carbon black that reduce the apparent crystalline order.

Raman spectra were collected for the graphite samples (G-pristine, G-slurry, G-470, G-450, and G-N100), revealing distinct structural variations among graphite samples subjected to different thermal treatments (Figure 5c). In the spectra, there are two main characteristic peaks, which represent the D band at 1355 cm^{-1} and the G band at 1575 cm^{-1}. The D band originates as a result of the presence of defects in the graphite structure causing a theoretically forbidden vibrational mode (graphene ring breathing A_{1g}) to become observable.[44] The ratio of the D peak to the G peak (which itself is associated with E_{2g} in-plane stretching and is not theoretically forbidden in perfect graphite) is a powerful tool for information about the disorder of the materials.[45]

The G-pristine spectra contain extremely weak intensity D bands, resulting in low I_D/I_G ratios (Figure 5d). This is indicative of highly ordered, crystalline graphite samples with very few defects present, and the narrow range of values of this ratio highlights the homogeneity of the sample. Comparatively, the Raman spectra of carbon black contain far more intense D bands and have I_D/I_G ratios in the range 2.2–3.2. Such ratios are characteristic of distorted, nanosized graphitic sheets (approx. 2 nm) with a high concentration of defects.[45] As is expected, the Raman spectra of G-slurry were further deviated from monocrystalline graphite than G-pristine, which is confidently attributed to the presence of carbon black in this sample.

Downloaded from pubs.acs.org/asmcd/article-pdf/3/8/2751/6650751 6/rm-2026-00237h.pdf by UNIV OF BATH user on 29 October 2026

https://doi.org/10.1021/acssusresmgt.6c00237
ACS Sustain. Resour. Manag. 2026, 3, 2751−2765

A wide range of I_D/I_G ratios were observed (0.1–0.7), resulting from a combination of the particulate nature of carbon black and the highly localized nature of Raman spectroscopy (Figure 5d).

For G-N100, I_D/I_G ratios observed are similar in value and distribution to those of G-pristine. This highlights the successful recovery of graphite, which is not significantly damaged compared with the original material, with CMC/SBR additives no longer present. Despite the low I_D/I_G ratios, these spectra showed the emergence of the D' peak at ~1615 cm^{-1} which is associated with the presence of "amorphous graphite". The amorphous carbon component observed in G-N100 likely arises from two contributing factors. Primarily, there remains some carbon black in the sample of graphite after NIR treatment, which is shown to have large D' peaks present in its Raman spectra. The Raman and PXRD data provide evidence that each of the methodologies outlined for graphite recovery successfully recovers material, which is similar in crystallinity to the original pristine graphite. In each case, there is an indication that a small amount of defective graphite exists. The origins of this disordered graphite predominantly arise from the presence of carbon black, and not due to structural damage.

3.4. Electrochemical Performance Evaluations

The cycle performance of G-pristine, G-slurry, G-470, G-450, and G-N100 at cycling currents of both 10 and 40 mA g^{-1} are shown in Figure 6 and Table 2. The electrochemical performances of G-470, G-450, and G-N100 as prospective anode materials were investigated, selected due to the complete removal of CMC and SBR as highlighted from the TGA trace (Figure 3b,c). Additionally, G-pristine was tested as a control and G-slurry is tested to assess the effect of any remaining CMC and SBR on the anode performances. The specific capacity of G-pristine was shown to be 356 mAh g^{-1} when cycled at a rate of 10 mA g^{-1}, which is lower than the theoretical capacity of graphite of 372 mAh g^{-1} (likely due to the quality of graphite selected). The initial specific capacity of G-slurry was 324.0 mAh g^{-1} but quickly deteriorated, losing 238.7 mAh g^{-1} after 20 cycles. The observed degradation is attributed to residual binder coverage in the G-slurry sample, which blocks active sites (as evidenced by the lower SSA) resulting in lower initial capacity.[46] It is likely that these blocked sites reduce the uniformity and therefore the stability of the SEI formation, leading to capacity fade in the G-slurry sample.[43] The poor performance from G-slurry in comparison to that of G-pristine highlights the need for full removal of any additives from a recovered anode material prior to its reuse. Both G-470 and G-450 achieved specific capacities of 374.7 and 373.7 mA g^{-1} at a cycle rate of 10 mA g^{-1}, and this exceeds the capacity of G-pristine (Table 2). An increase in capacity following thermal reprocessing of graphite (exceeding the theoretical capacity) has been reported in several graphite recycling studies;[47−50] this has generally been attributed to both an improvement in the crystallite ordering increases accessible interlayer sites and increased edge defects. Improved crystallite ordering is indicated by our Raman and XRD data; furnace-treated samples exhibit lower ID/IG ratios and d_{002} values closer to pristine graphite, indicating improved stacking order, maximizing the number of fully accessible interlayer galleries available for reversible lithiation. While this improves the capacity, it is the increase in defect sites, as indicated by the higher surface area (Figure 4f), that is the likely cause of capacity increases beyond the theoretical capacity; this is an open area for further research to understand better the mechanism of capacity increase.

In the case of the thermally treated samples, the increase in capacity of G-470 and G-450 occurred alongside an increase

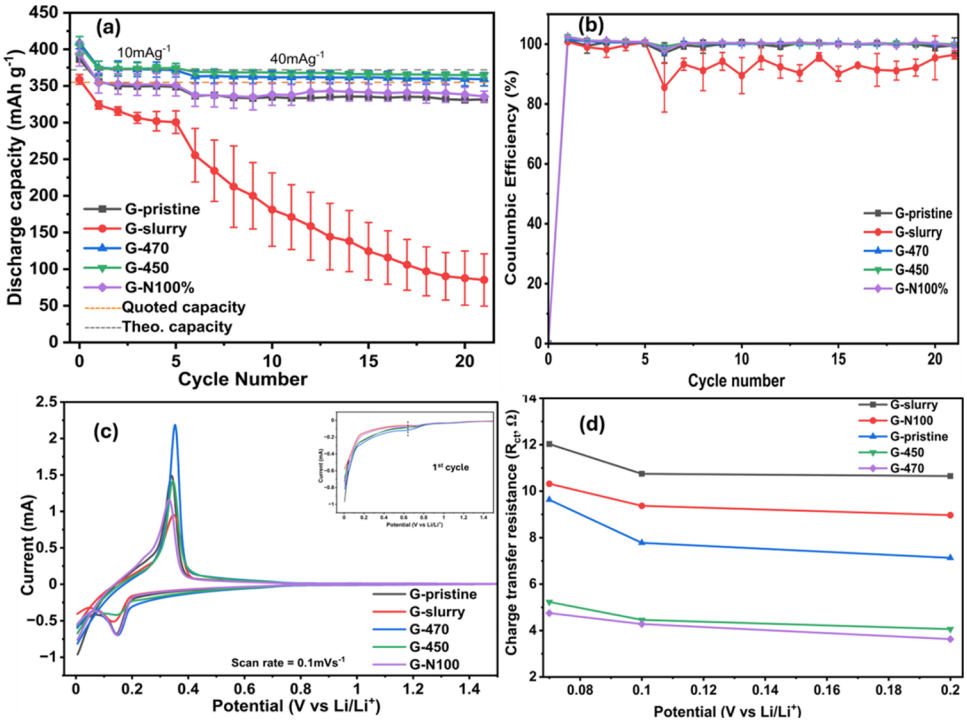


Figure 6. Cyclic performance curves showing (a) discharge capacity (e.g., lithium extraction), (b) coulombic efficiency curves, (c) cyclic voltammetry curves, and (d) and evolution of charge transfer resistance (R_{ct}) with potential of G-pristine, G-slurry, G-470, G-450, and G-N100.

Downloaded from pubs.acs.org/asmcd/article-pdf/3/8/2751/6507516/rm-2026-00237h.pdf by UNIV OF BATH user on 29 October 2026

https://doi.org/10.1021/acssusresmgt.6c00237
ACS Sustain. Resour. Manag. 2026, 3, 2751−2765

Table 2. First Cycle Losses, Capacity Losses, and Coulombic Efficiency after 20 Cycles[a]

Material	1st irreversible discharge capacity	1st charge capacity	1st reversible discharge capacity	capacity loss after 20 cycles		Coulombic efficiency after 20 cycles
	(mA h g^{-1})	(mA h g^{-1})	(mA h g^{-1})	mA h g^{-1}	% loss	(%)
G-pristine	386.5 ± 11.8	351.6 ± 11.7	356.0 ± 10.4	30.0 ± 16.1	8.43 ± 4.55	97.7 ± 2.50
G-slurry	359.0 ± 6.56	321.5 ± 6.24	324.0 ± 5.37	238.7 ± 28.0	73.7 ± 8.81	96.5 ± 1.41
G-470	409.0 ± 8.31	368.9 ± 7.95	374.7 ± 9.11	15.4 ± 4.76	4.10 ± 1.26	99.9 ± 0.14
G-450	405 ± 12.6	364.9 ± 12.6	373.7 ± 10.3	8.78 ± 5.89	2.32 ± 0.15	99.9 ± 0.06
G-N100	393.9 ± 16.8	338.6 ± 9.77	354.1 ± 13.6	18.3 ± 5.60	5.12 ± 1.43	99.5 ± 0.68

[a]Each sample was tested using three half-cells; therefore, each data point is an average with its standard error between three cells.

in the ordering of the graphitic layers compared with G-pristine, as evidenced by the I_D/I_G ratios from the Raman spectra (Figure 5d). The electrochemical results and similar physical characterization highlight both thermal treatments as robust methods of material recovery for graphite-based anodes. G-N100 provided a specific capacity of 354.1 mAh g^{-1} at 10 mA g^{-1} and 337.5 mAh g^{-1} at 40 mA g^{-1}, which are comparable to the capacity of the G-pristine at the equivalent current densities (Figure 6a), suggesting that the graphite had been recovered effectively, avoiding significant damage to the material. However, the capacities of both G-pristine and G-N100 were both below the theoretical capacity of 372 mAh g^{-1}, indicating that within the tested parameters, the NIR process did not improve the graphitic order of the graphite compared to thermal treatment. Although the performance of G-N100 was slightly less impressive (along with an increase in I_D/I_G ratio), these results are promising in the context of a low-energy recovery method.

Figure 6b presents the coulombic efficiency (CE) for all cycled cells. The CE values remained consistently high, around 99%, for all cells after 20 cycles, except for the G-slurry, which showed fluctuations and thus poor overall performance. The low CE at the start of cycling and the substantial first-discharge capacity loss observed in Table 2 are associated with the initial formation of the SEI layer via reductive decomposition of the electrolyte at the graphite surface.[51] The SEI layer facilitates Li-ion passivation of the graphite surface during cycling. After the first lithiation, subsequent charge–discharge processes become reversible for G-pristine, G-470, G-450, and G-N100, indicating the formation of a stable SEI layer. In contrast, the SEI layer for G-slurry was observed to be unstable, leading to rapid, large capacity loss within a few cycles.

To understand further the effect of thermal treatment on the electrochemical performance of the graphite anode, CV tests were performed on all samples at a scan rate of 0.1 mV s^{-1}. Figure 6c presents the CV curves for G-pristine, G-slurry, G-470, G-450, and G-N100 during the lithium intercalation/deintercalation process in the potential window of 0 to 1.5 V vs Li/Li^+. In the first charge–discharge cycle, a reduction peak appeared near 0.64 V for all samples (Figure 6c inset). This peak is commonly ascribed to the irreversible formation of the SEI prior to Li intercalation into the graphite. Notably, this peak diminished in subsequent cycles, indicating stabilization of the SEI film. As the potential was scanned toward lower values, a pair of prominent oxidation–reduction peaks were observed at approximately 0.15 and 0.35 V. These peaks correspond to the intercalation and deintercalation of Li^+ in the graphite structure. Among the samples, G-470 exhibits the largest peak current, followed by G-pristine, G-450, and G-N100, with G-slurry showing the smallest current. The magnitude of the peak current reflects the apparent reaction rate and suggests that graphite subjected to thermal treatment exhibited enhanced electrochemical reactivity.[52] Relative to G-slurry, the thermally treated samples (G-470 and G-450) and G-N100 showed higher correspondence of the oxidation–reduction peaks, with smaller potential separation (ΔE). This reduced peak-to-peak separation indicates lower electrode polarization and improved reaction reversibility during the lithiation/delithiation processes after treatment.

EIS was used to examine further the electrochemical performance differences of these samples. EIS data were collected on half cells made from G-pristine, G-slurry, G-450, G-470, and G-N100 at both open circuit and under bias (Figures S12–S16). An equivalent circuit model was used and employed to fit the data using non-linear least squares fits the impedance data to extract parameters, and the residual standard error was found to be $\leq 10^{-3}$.

The semicircle assignments and hence time constants are based on the frequency window related to the physical electrochemical process, as reported in the literature,[53−57] and these are summarized in Table 3.

The ECM consisted of different block combinations connected in series. An ohmic resistance (RΩ) connected to a first block built from a constant phase element (CPE) in parallel with a contact resistance representing the larger interfacial resistance measured at the electrode-current collector interface. This block in turn was connected to a second CPE in parallel with a resistance (RSEI) representing the SEI block. Last, the third block is a constant phase element in parallel with a charge transfer resistance (R_{ct}) and a Warburg diffusion element (W) representing a so-called Randles circuit. Figure 6d shows the evolution of R_{ct} with potential, as well as exhibiting the effect

Table 3. Frequency Range Attributed to Different Physical Electrochemical Processes

Frequency range (Hz)	Physical electrochemical process
>10 kHz (ultra high)	Time constant related to contact resistance and interface constraints (electrode to current collector), and inductive effects
100 Hz–10 kHz (High)	Time constant related to SEI film resistance and capacitance
100 mHz–100 Hz (medium)	Time constant related charge transfer resistance (R_{CT}) and the double-layer capacitance
<100 mHz (low)	Diffusion process

https://doi.org/10.1021/acssusresmgt.6c00237
ACS Sustain. Resour. Manag. 2026, 3, 2751−2765

Downloaded from pubs.acs.org/asmcd/article-pdf/3/8/2751/6650751 6/rm-2026-00237h.pdf by UNIV OF BATH user on 29 October 2026

of the different treatments. As a general observed trend, R_{ct} decreased nonlinearly with increasing potential; at OCP, the net current is zero and lithiation balances with delithiation. In this condition, the exchange current density is at equilibrium and a minimum value that results in a maximum possible R_{ct} as per eq 1, where R = gas constant, T = temperature, n = number of electrons in reaction, F = Faradays constant, and i_0 = exchange current density.

$$R_{ct} = \frac{RT}{nFi_0} \quad (1)$$

Under bias, there is an increase in availability of reactive sites and changes in lithium concentration leading to exchange current density increases and therefore the observed decrease in R_{ct}.

For the different materials investigated, R_{ct} can be ranked as follows: G-slurry > G-N100 > G-pristine > G-450 > G-470. The charge transfer resistance R_{ct} indicates effective cell performance and efficiency. It is associated with the resistance at the electrode–electrolyte interface redox process (i.e., electron transfer), high R_{ct} will impede lithium-ion movement, and conversely, lower R_{ct} implies that electrons are transferred more easily. The greater the resistance, the slower the kinetics, and this relates very well with the performance observed in terms of capacity displayed on first charge/ discharge (Table 2).

Energy and Environmental Considerations

This work is intended to demonstrate that organic binders can be removed from graphite anode materials at rates >200 times faster than conventional furnaces without causing damage to the graphite, which would make it unsuitable for reuse as a battery anode material. Using this lab-based machine and conditions outlined in the experimental methods, the energy required to process 1 kg of anode material is calculated to be 1.54 kWh, although graphite loading has not been optimized and could potentially be processed at a much higher density than in this work. The lab-based machine has not been optimized for efficiency but for versatility within a research environment spanning processing of steel, metal oxides, perovskites, adhesives, and recycling. The most effective way to improve the efficiency is to improve the view factor of the machine by bringing the lamps closer to the sample. The machine could be modified to reduce the 6 cm standoff distance to 1.5 cm; this would almost double the view factor from 0.19 to 0.35[29] and reduce by the same factor the energy needed for the equivalent heating effect. Additional improvements could be made by including polished aluminium reflectors as used in industrial NIR machines, such as those that cure steel coatings at in industrial steel plants.[58]

Beyond energy use, it is worth noting that the processing of this 100 kg could be undertaken on a lab-based machine with a footprint of <1 m^2 presenting significant opportunities for scale-up. Alternatively, its small size allows it to be sited where the manufacturing waste is produced, reducing transport costs/emissions and enabling on-site material recovery within a factory environment. Because there is no requirement to hold the machine at temperature to improve efficiency, there is opportunity for load shifting, e.g., processing waste when power prices are low and stopping the process at peak times.

The direct emissions come from two sources, combustion of organics and energy use. Scope 1 emissions from the complete decomposition of CMC, SBR, and CB leads to CO_2 emissions of 1.6, 3.67, and 3.3 $kgCO_2/kg$, respectively, these cannot be reduced by process optimization (Table S3). Figure 7 compares the emissions for 1 kg of reprocessed graphite in our current setup and an optimized lab system using UK 2025 grid[59] carbon dioxide equivalent values (CO_{2e}) and a 90% graphite yield; the emissions for producing battery anode graphite using a primarily hydroelectric power grid (Quebec) are included for comparison since this represents some of the lowest emissions pristine material production (1.4 kg CO_{2e}/kg). An equivalent material produced in China has an emissions factor of 9.6 $kgCO_{2e}/$

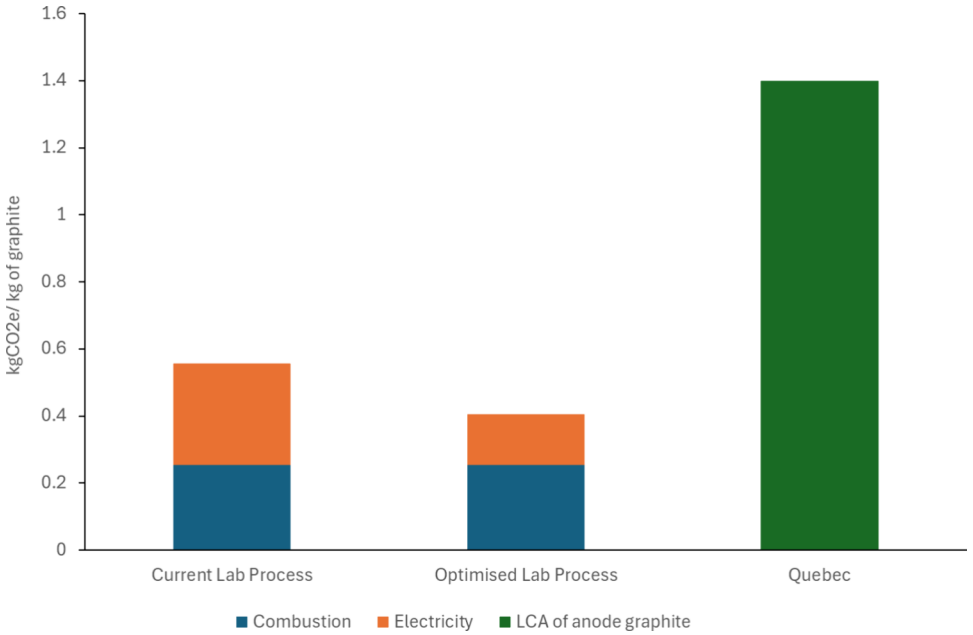


Figure 7. Greenhouse gas emissions of recovering 1 kg of anode grade graphite through this process, an optimized lab process, and through mining and spheroidalizing in Quebec.[60]

Downloaded from pubs.acs.org/asmcd/article-pdf/3/8/2751/6650751 6/rm-2026-00237h.pdf by UNIV OF BATH user on 29 October 2026

https://doi.org/10.1021/acssusresmgt.6c00237
ACS Sustain. Resour. Manag. 2026, 3, 2751−2765

kg.[60] The decomposition emissions are ~50% of the CO_2 emissions in the lab system, and with only minor optimization, these drop to become less than a third of total emissions to 0.4 kg CO_{2e}/kg of graphite, comparing favorably with recycling end-of-life graphite, which can range where leaching methods are typically >2 kgCO_{2e}/kg and microwave processing can be 9.7 kgCO_{2e}/kg.[61]

Table 4 compares this work with other literature recovering graphite from LIB scrap and EOL cells. While thermal methods are the most common and if undertaken in an N_2 atmosphere can have low emissions,[62] the long residence times lead to reduced throughput.

4. CONCLUSIONS

This study presents a new NIR thermal approach for graphite regeneration from a slurry, thereby offering an inline alternative to conventional furnace-based recycling methods. The results demonstrate that both conventional furnace treatment at 450–470 °C for 60–120 min and NIR irradiation at 100% intensity for only 15.6 s can effectively remove the binders without compromising the graphite crystal structure. While conventional furnace treatment effectively decomposed SBR and CMC binders at elevated temperatures, it required prolonged heating, whereas near-infrared irradiation provided comparable binder removal within seconds, highlighting its superiority in terms of processing efficiency.

Detailed physical characterization that involved XRD and SEM morphology analysis revealed that the post-treatment graphite retained its crystallinity and flake-like morphology. Raman spectroscopy analysis indicates that furnace treatment restored graphite to near-pristine quality while NIR-treated graphite showed a slightly higher I_D/I_G than the pristine material, suggesting some residual amorphous or minor disorder carbon, but markedly improved relative to the untreated slurry.

NIR-regenerated graphite delivered an initial specific capacity of 354.1 mAh g^{-1} at 10 mA g^{-1} and retained 99.9% of its capacity after 20 cycles. This specific capacity was close to 99.4% of the pristine graphite (356.0 mAh g^{-1}), highlighting the effectiveness of the binder removal and preservation of the graphitic structure. The furnace-regenerated samples exhibited higher specific capacities of 374.7 and 373.7 mAh g^{-1} at 10 mA g^{-1}, exceeding that of pristine graphite. While conventional furnace treatments achieved higher specific capacities, these gains come at the expense of prolonged processing time. In contrast, the new ultrafast NIR process offers a compelling balance between performance preservation and process speed, highlighting its suitability for high-throughput, closed-loop recycling systems. The findings underscore that complete binder removal is sufficient to restore graphite functionality, opening new pathways for low-impact anode recycling.

Overall, this work positions NIR-based thermal regeneration as a potentially transformative technology for sustainable manufacture of lithium-ion batteries, with the capacity to reduce recycling energy demand, lower material costs, and improve the circularity of critical battery materials. It is a technology that is scalable, suitable for inline production, and ultra-fast, and its adoption could play a key role in enabling next-generation battery supply chains that are both economically and environmentally resilient.

5. FURTHER RESEARCH

The NIR process has the potential for scale-up and automation, in a continuous-flow process for commercialization; however, it requires further work to raise its Technology Readiness Level (TRL). This paper serves as a proof of concept on recycling manufacturing waste, validating the application of the technology at TRL 3. To apply the technology to end-of-life cells, the SEI layer and other contaminants from the cell need to be considered, while most contaminants are likely to decompose under NIR processing Li_2O and LiF are likely to remain which may require solvent treatment to fully remove, either before or after thermal processing.

It is a technology that could enable value to be preserved from end-of-life lithium-ion cells, rather than destroying it through "downcycling".[68] The approach is best suited to large, planar electrodes, such as those found in cell-to-pack, and pouch cells, and is unlikely to find industrial application with smaller cells or cylindrical cells because of the challenges presented by disassembly.

Table 4. Summary of Graphite Recovery Methods for LIB Scrap and EOL Cells

method	role in recovery chain	principle	feedstock	outcome	advantages	limitations	ref
mechanical liberation	pre-treatment	size reduction/ delamination	LIB scrap/ electrode waste	partially liberated composite	low cost, scalable	incomplete separation of binder/graphite	Gaines[63]
NIR-assisted thermal treatment (this work)	binder removal	near-infrared radiation induces rapid localized heating → decomposition/ softening of organic binders (e.g., CMC, SBR, and PVDF)	waste graphite electrodes/ anode scrap	binder-free or binder-reduced graphite particles	fast heating, selective organic removal, dry process	requires energy optimization- untested on EOL graphite	this work
ultrasonic removal	separation of different cell components	ultrasonic separation	mixed black mass waste	partially liberated composite	low temperature	not proven in cells, some binder, may remain adhered to graphite	Badenhorst et al.[64]
hydrometallurgical leaching	purification	dissolution of metal impurities	black mass/ recovered solids	high-purity graphite	high purity product	chemical waste, multi-step	Liang et al.[65]
thermal pyrolysis (conventional)	binder removal	furnace heating (bulk heating)	scrap electrodes	binder decomposition	effective but slow	long residence time	He et al.,[66] Ma et al.,[67] and Nataragan et al.[62]

https://doi.org/10.1021/acssusresmgt.6c00237
ACS Sustain. Resour. Manag. 2026, 3, 2751−2765

Downloaded from pubs.acs.org/asmcd/article-pdf/3/8/2751/6650751 6/rm-2026-00237h.pdf by UNIV OF BATH user on 29 October 2026

In order to realize the potential of this technology, lithium-ion recycling systems need to transition from crude mechanical handling, reliant on comminution, to pack, module, and cell disassembly[69] in order to enable high-value materials recovery. Automated disassembly is seen as a key enabler for high-throughput end-of-life processing.[70]

Many technology roadmaps for lithium-ion recycling envisage a future where batteries are disassembled, rather than shredded.[71,72] A key enabler of this future circular economy is consideration of end-of-life requirements at the design stage to ease disassembly.[73] Many of the batteries presently on the marketplace are not optimized for disassembly,[73] and there remains enormous scope for "Design for Recycle" thinking at the manufacturing stage to make batteries easier to recycle at the end of life.

■ ASSOCIATED CONTENT

Supporting Information

The Supporting Information is available free of charge at https://pubs.acs.org/doi/10.1021/acssusresmgt.6c00237.

NIR process and modeling of the system, TGA plots for the different processed materials , EIS plots for the tested cells, and summary of the GHG emissions factors for different processing options (PDF)

■ AUTHOR INFORMATION

Corresponding Author

Jenny Baker – *Faculty of Engineering and Design, University of Bath, Bath BA2 7AY, UK; Faculty of Science and Engineering, Swansea University, Bay Campus, Swansea SA1 8EN, UK;* orcid.org/0000-0003-3530-1957; Email: JB4251@bath.ac.uk

Authors

Wafaa Al-Shatty – *Faculty of Engineering and Design, University of Bath, Bath BA2 7AY, UK; Faculty of Science and Engineering, Swansea University, Bay Campus, Swansea SA1 8EN, UK*

Oriyomi O. Ogunbanjo – *School of Chemistry, University of Birmingham, Edgbaston Campus, Birmingham B15 2TT, UK; Birmingham Centre for Strategic Elements & Critical Materials, University of Birmingham, Edgbaston Campus, Birmingham B15 2TT, UK*

Harrison Fell – *School of Chemistry, University of Birmingham, Edgbaston Campus, Birmingham B15 2TT, UK; Birmingham Centre for Strategic Elements & Critical Materials, University of Birmingham, Edgbaston Campus, Birmingham B15 2TT, UK*

Oli Fryatt – *Faculty of Engineering and Design, University of Bath, Bath BA2 7AY, UK*

Pierrot S. Attidekou – *School of Chemistry, University of Birmingham, Edgbaston Campus, Birmingham B15 2TT, UK; Birmingham Centre for Strategic Elements & Critical Materials, University of Birmingham, Edgbaston Campus, Birmingham B15 2TT, UK; The Faraday Institution, Quad One, Harwell Science and Innovation Campus, Didcot OX11 0RA, UK*

Gavin Harper – *School of Chemistry, University of Birmingham, Edgbaston Campus, Birmingham B15 2TT, UK; Birmingham Business School, University of Birmingham, Edgbaston Campus, Birmingham B15 2TT, UK; Birmingham Centre for Strategic Elements & Critical Materials, University of Birmingham, Edgbaston Campus, Birmingham B15 2TT, UK; The Faraday Institution, Quad One, Harwell Science and Innovation Campus, Didcot OX11 0RA, UK;* orcid.org/0000-0002-4691-6642

Paul A. Anderson – *School of Chemistry, University of Birmingham, Edgbaston Campus, Birmingham B15 2TT, UK; Birmingham Centre for Strategic Elements & Critical Materials, University of Birmingham, Edgbaston Campus, Birmingham B15 2TT, UK; The Faraday Institution, Quad One, Harwell Science and Innovation Campus, Didcot OX11 0RA, UK*

Davide Deganello – *Faculty of Science and Engineering, Swansea University, Bay Campus, Swansea SA1 8EN, UK;* orcid.org/0000-0001-8341-4177

Complete contact information is available at: https://pubs.acs.org/doi/10.1021/acssusresmgt.6c00237

Author Contributions

The manuscript was written through contributions of all authors. All authors have given approval to the final version of the manuscript. Conceptualization: Wafaa Al–Shatty, Jenny Baker, Davide Deganello, and Paul A. Anderson. Validation/investigation: Wafaa Al–Shatty, Oriyomi O. Ogunbanjo, Harrison Fell, and Pierrot S. Attidekou. Writing of original draft, Wafaa Al–Shatty, Jenny Baker, Oriyomi O. Ogunbanjo, and Harrison Fell. Writing–review and editing: Wafaa Al–shatty, Jenny Baker, Paul Anderson, Oriyomi O. Ogunbanjo, Harrison Fell, and Davide Deganello. Modeling of the NIR process: Oli Fryatt. Funding acquisition: Jenny Baker, Gavin Harper and Paul Anderson.

Notes

The authors declare no competing financial interest.

■ ACKNOWLEDGMENTS

We acknowledge funding from the EPSRC ECR Fellowship NoRESt EP/S03711X/1 (W-.A.S. and J.B.) and TReFCo EP/W019167/2 (W-.A.S., D.D., J.B., O.O., H.F., P.A.A., and G.H.), and Faraday Institution grant FIRG085 (G.H., P.A.A., and P.S.A.). The authors would like to thank Swansea University for access to characterization equipment at the Swansea University Advanced Imaging of Materials (AIM) facility, which was funded in part by the EPSRC (EP/M028267/1) and the European Regional Development Fund through the Welsh Government (80708).

■ REFERENCES

(1) Chen, M.; Ma, X.; Chen, B.; Arsenault, R.; Karlson, P.; Simon, N.; Wang, Y. Recycling End-of-Life Electric Vehicle Lithium-Ion Batteries. *Joule* **2019**, *3* (11), 2622–2646.

(2) Yang, Y.; Okonkwo, E. G.; Huang, G.; Xu, S.; Sun, W.; He, Y. On the sustainability of lithium ion battery industry – A review and perspective. *Energy Storage Mater.* **2021**, *36*, 186–212.

(3) Walton, A. A.; Paul, A.; Harper, G.; Mann, V.; Beddington, J.; Abbott, A.; Bloodworth, A.; OudeNijeweme, D.; Schofield, E.; Wall, F.; Glover, N.; Chaddock, R.; Gross, R.; Lee, R.; Grimes, R.; Lewis, R.; Gibson, V.; McGuiness, P.; Ogrin, R. *Securing technology-critical metals for Britain*; University of Birmingham, Birmingham Centre for Strategic Elements & EPSRC Critical Materials & Critical Elements and Materials (CrEAM) Network (**2021**).

(4) Li, Y.; Lv, W.; Huang, H.; Yan, W.; Li, X.; Ning, P.; Cao, H.; Sun, Z. Recycling of spent lithium-ion batteries in view of green chemistry *Green Chem.* **2021**, *23* (17), 6139–6171.

Downloaded from pubs.acs.org/asmod/article-pdf/3/8/2751/6507516/rm-2026-00237h.pdf by UNIV OF BATH user on 29 October 2026

(5) Dobó, Z.; Dinh, T.; Kulcsár, T. A review on recycling of spent lithium-ion batteries. *Energy Rep.* **2023**, *9*, 6362–6395.
(6) Dunn, J.; Kendall, A.; Slattery, M. Electric vehicle lithium-ion battery recycled content standards for the US – targets, costs, and environmental impacts. *Resour. Conserv. Recycl.* **2022**, *185*, No. 106488.
(7) Li, P.; Luo, S.; Zhang, L.; Liu, Q.; Wang, Y.; Lin, Y.; Xu, C.; Guo, J.; Cheali, P.; Xia, X. Progress, challenges, and prospects of spent lithium-ion batteries recycling: A review. *J. Energy Chem.* **2024**, *89*, 144–171.
(8) Baum, Z. J.; Bird, R. E.; Yu, X.; Ma, J. Lithium-Ion Battery Recycling—Overview of Techniques and Trends. *ACS Energy Lett.* **2022**, *7* (2), 712–719.
(9) Intelligence, B.M. *Infographic: China controls three-quarters of graphite anode supply chain* (accessed 01/03/2026).
(10) Zhang, J.; Liang, C.; Dunn, J. B. Graphite Flows in the U.S: Insights into a Key Ingredient of Energy Transition. *Environ. Sci. Technol.* **2023**, *57* (8), 3402–3414.
(11) BanQu *The Critical Raw Materials Guide: How to Stay Compliant with EU & U.S Regulations* (**2024**) https://www.banqu.co/blog/the-critical-raw-materials-guide#strongdata-amp-reporting-for-sustainably-sourced-critical-raw-materialsstrong.
(12) Venditti, B.; Aboulazm, Z. *The Critical Minerals to China, EU, and U.S. National Security Element* (**2023**) https://elements.visualcapitalist.com/the-critical-minerals-to-china-eu-and-u-s-national-security/.
(13) Sommerville, R.; Shaw-Stewart, J.; Goodship, V.; Rowson, N.; Kendrick, E. A review of physical processes used in the safe recycling of lithium ion batteries. *Sustain. Mater. Techno.* **2020**, *25*, No. e00197.
(14) Yu, L.; Bai, Y.; Polzin, B.; Belharouak, I. Unlocking the value of recycling scrap from Li-ion battery manufacturing: Challenges and outlook. *J. Power Sources* **2023**, *593*, No. 233955.
(15) Sargent, A. T.; Henderson, Z.; Walton, A. S.; Spencer, B. F.; Sweeney, L.; Flavell, W. R.; Anderson, P. A.; Kendrick, E.; Slater, P. R.; Allan, P. K. Reclamation and reuse of graphite from electric vehicle lithium-ion battery anodes via water delamination. *J. Mater. Chem. A* **2023**, *11* (17), 9579–9596.
(16) Roy, J. J.; Phuong, D. M.; Verma, V.; Chaudhary, R.; Carboni, M.; Meyer, D.; Cao, B.; Srinivasan, M. Direct recycling of Li-ion batteries from cell to pack level: Challenges and prospects on technology, scalability, sustainability, and economics. *Carbon Energy* **2024**, *6* (6), No. e492.
(17) Zhang, G.; He, Y.; Feng, Y.; Wang, H.; Zhu, X. Pyrolysis-Ultrasonic-Assisted Flotation Technology for Recovering Graphite and $LiCoO_2$ from Spent Lithium-Ion Batteries. *ACS Sustain. Chem. Eng.* **2018**, *6* (8), 10896–10904.
(18) Natarajan, S.; Boricha, A. B.; Bajaj, H. C. Recovery of value-added products from cathode and anode material of spent lithium-ion batteries. *Waste Manag.* **2018**, *77*, 455–465.
(19) Yu, J.; He, Y.; Ge, Z.; Li, H.; Xie, W.; Wang, S. A promising physical method for recovery of $LiCoO_2$ and graphite from spent lithium-ion batteries: Grinding flotation. *Sep. Purif. Technol.* **2018**, *190*, 45–52.
(20) Peng, J.; Maslek, S.; Sharma, N. Spent graphite from lithium-ion batteries: re-use and the impact of ball milling for re-use. *RSC Sustain.* **2024**, *2* (5), 1418–1430.
(21) Lombardo, G.; Ebin, B.; St. J. Foreman, M. R.; Steenari, B.-M.; Petranikova, M. Chemical Transformations in Li-Ion Battery Electrode Materials by Carbothermic Reduction. *ACS Sustainable Chem. Eng.* **2019**, *7* (16), 13668–13679.
(22) Mannu, A.; Di Pietro, M. E.; Bosello, V.; Mulas, G.; Ferrario, C.; Murgia, F.; Foddai, A. F.; Magugliani, G.; Mossini, E.; Macerata, E.; et al. Selective and sustainable recovery of lithium from black mass via microwave and green leaching techniques. *Mater. Sci. Eng.: B* **2026**, *323*, No. 11873.
(23) Yu, H.; Dai, H.; Zhu, Y.; Hu, H.; Zhao, R.; Wu, B.; Chen, D. Mechanistic insights into the lattice reconfiguration of the anode graphite recycled from spent high-power lithium-ion batteries. *J. Power Sources* **2021**, *481*, No. 229159.
(24) Gao, Y.; Zhang, J.; Jin, H.; Liang, G.; Ma, L.; Chen, Y.; Wang, C. Regenerating spent graphite from scrapped lithium-ion battery by high-temperature treatment. *Carbon* **2022**, *189*, 493–502.
(25) Pražanová, A.; Kočí, J.; Uřičář, J.; Pilnaj, D.; Stroe, D.-I.; Knap, V. Optimized Thermal Treatment of Lithium-Ion Battery Components as a Basis for Sustainable Pyrometallurgy. *ChemSusChem* **2025**, *18* (24), No. e202501753.
(26) Griffin, R.; Hooper, K.; Charbonneau, C.; Baker, J. Comparative Study of Radiative Heating Techniques for Fast Processing of Functional Coatings for Sustainable Energy Applications. *Johns. Matthey Technol. Rev.* **2022**, *66* (1), 32–43.
(27) Baker, J.; Hooper, K.; Meroni, S.; Pockett, A.; McGettrick, J.; Wei, Z.; Escalante, R.; Oskam, G.; Carnie, M.; Watson, T. High throughput fabrication of mesoporous carbon perovskite solar cells *J. Mater. Chem. A* **2017**, *5* (35), 18643–18650.
(28) Brennan, D. A. *Computational and Experimental Study on Near-infrared Heating for the Coil Coating Industry*. Ph.D Thesis; Swansea University, **2018**.
(29) Abasi, S.; Minaei, S.; Jamshidi, B.; Fathi, D. Development of an Optical Smart Portable Instrument for Fruit Quality Detection. *IEEE Trans. Instrum. Meas.* **2021**, *70*, 1–9.
(30) Tyagi, L.; Sharma, G. P.; Verma, R. C.; Jain, S. K.; Murdia, L. K.; Mathur, S. M. Infrared heating in food processing: An overview. *Int. J. Chem. Stud.* **2020**, *8* (3), 327–336.
(31) Krishnamurthy, K.; Khurana, H. K.; Soojin, J.; Irudayaraj, J.; Demirci, A. Infrared Heating in Food Processing: An Overview. *Compr. Rev. Food Sci. Food Saf.* **2008**, *7* (1), 2–13.
(32) SPECIFIC. *How to Mix and Spread Hard Carbon Electrodes*, https://www.youtube.com/watch?v=aGeW6GPyTZ8 (accessed March 16, 2026).
(33) Valls, R. M.; Griffin, R.; Sawhney, A.; Domingos-Dlofo, C.; Dunlop, T.; Reis, S.; Holliman, P. J.; Baker, J. A new approach for obtaining ceramic NASICON ($Na_3Zr_2Si_2PO_{12}$) films sintered in situ by a sol–gel method, using spray deposition and near-infra red sintering. *J. Mater. Chem. A* **2024**, *12* (45), 31116–31120.
(34) Farivar, F.; Lay Yap, P.; Karunagaran, R. U.; Losic, D. Thermogravimetric Analysis (TGA) of Graphene Materials: Effect of Particle Size of Graphene, Graphene Oxide and Graphite on Thermal Parameters. *C* **2021**, *7*, No. 41.
(35) Zaghib, K.; Song, X.; Kinoshita, K. Thermal analysis of the oxidation of natural graphite: isothermal kinetic studies. *Thermochim. Acta* **2001**, *371* (1), 57–64.
(36) Nassar, M.; Bogomolov, K.; Grishina, E.; Ein-Eli, Y.; Amdursky, N. Towards eco-friendly batteries: high temperature baking of carbonaceous (MCMB) Li-ion anodes containing advanced water-based natural polymer binders results in superior performance. *J. Solid State Electrochem.* **2025**.
(37) Baker, J. A.; Worsley, C.; Lee, H. K. H.; Clark, R. N.; Tsoi, W. C.; Williams, G.; Worsley, D. A.; Gethin, D. T.; Watson, T. M. Development of Graphene Nano-Platelet Ink for High Voltage Flexible Dye Sensitized Solar Cells with Cobalt Complex Electrolytes. *Adv. Eng. Mater.* **2017**, *19* (3), No. 1600652.
(38) Oka, H. Electrochemical Properties of Unused Graphite Electrode Composite after Exfoliation and Recoating. *ACS Sustainable Chem. Eng.* **2025**, *13* (17), 6399–6411.
(39) Jiang, W.; Nadeau, G.; Zaghib, K.; Kinoshita, K. Thermal analysis of the oxidation of natural graphite – effect of particle size. *Thermochim. Acta* **2000**, *351* (1), 85–93.
(40) Gurzęda, B.; Buchwald, T.; Nocuń, M.; Bąkowicz, A.; Krawczyk, P. Graphene material preparation through thermal treatment of graphite oxide electrochemically synthesized in aqueous sulfuric acid *RSC Adv.* **2017**, *7* (32), 19904–19911.
(41) Cheng, N.; Cheng, X.; Fan, R.; Huang, F.; Li, S. Efficient regeneration of anode graphite from spent lithium-ion batteries using a deep eutectic solvent method. *J. Energy Storage* **2025**, *127*, No. 117168.
(42) Lähde, A.; Välikangas, J.; Meščeriakovas, A.; Karhunen, T.; Meščeriakovė, S.-M.; Sippula, O.; Leinonen, S.; Lassi, U.; Jokiniemi, J. Effect of high temperature thermal treatment on the electrochemical performance of natural flake graphite. *J. Mater. Res.* **2024**, *39* (6), 944–954.
(43) Yu, R.; Zhou, C.; Zhou, X.; Yang, J.; Tang, J.; Zhang, Y. Efficient Regeneration of Graphite from Spent Lithium-Ion Batteries through

Downloaded from pubs.acs.org/asmcd/article-pdf/3/8/2751/6650751 6/rm-2026-00237h.pdf by UNIV OF BATH user on 29 October 2026

Combination of Thermal and Wet Metallurgical Approaches. *Materials* **2024**, *17* (16), No. 3883.
(44) Tuinstra, F.; Koenig, J. L. Raman Spectrum of Graphite. *J. Chem. Phys.* **1970**, *53* (3), 1126–1130.
(45) Ferrari, A. C.; Robertson, J. Interpretation of Raman spectra of disordered and amorphous carbon. *Phys. Rev. B* **2000**, *61* (20), 14095–14107.
(46) Zeng, G.; Zhou, R.; Hu, C.; Zhao, H.; Gao, H.; Huang, J.; Yu, J.; Luo, F.; Wang, Z.; Deng, C.; et al. Recycling of graphite from spent lithium–ion batteries via low-temperature polyvinyl chloride roasting-assisted leaching. *Carbon* **2025**, *238*, 120182.
(47) Wei, X.; Guo, Z.; Zhao, Y.; Sun, Y.; Hankin, A.; Titirici, M. Recovery of graphite from industrial lithium-ion battery black mass. *RSC Sustainability* **2025**, *3*, 264.
(48) Dong, S.; Song, Y.; Ye, K.; et al. Ultra-fast, low-cost, and green regeneration of graphite anode using flash joule heating method. *EcoMat* **2022**, *4* (5), No. e12212.
(49) Ji, S.; Zhang, A.; Hua, W.; Yan, S.; Chen, X. Regeneration of graphite from spent lithium-ion batteries as anode materials through stepwise purification and mild temperature restoration. *Battery Energy* **2024**, *3*, No. 20230067.
(50) Ma, X.; Chen, M.; Chen, B.; Meng, Z.; Wang, Y. *ACS Sustainable Chem. Eng.* **2019**, *7*, 24, 19732–19738.
(51) Sen, A.; Kumar, K.; Kumar, S.; Ghanty, C.; Mahato, S.; Dash, P. S.; Biswas, K.; Kundu, R. Reviving Graphite Anode from Spent Li-Ion Batteries via Acid Leaching and Carbonization Methodology. *ACS Sustainable Resour. Manage* **2025**, *2* (4), 642–650.
(52) Yu, G. Q.; Xie, M. Z.; Zheng, Z. H.; Wu, Z. G.; Zhao, H. L.; Liu, F.-Q. Efficiently regenerating spent lithium battery graphite anode materials through heat treatment processes for impurity dissipation and crystal structure repair. *Resour. Conserv. Recycl.* **2023**, *199*, No. 107267.
(53) Weber, R.; Louli, A. J.; Plucknett, K. P.; Dahn, J. R. Resistance Growth in Lithium-Ion Pouch Cells with $LiNi_{0.80}Co_{0.15}Al_{0.05}O_2$ Positive Electrodes and Proposed Mechanism for Voltage Dependent Charge-Transfer Resistance. *J. Electrochem. Soc.* **2019**, *166*, No. A1779.
(54) Hiroki, N.; Mukoyama, D.; Shimizu, R.; Momma, T.; Osaka, T. Systematic analysis of interfacial resistance between the cathode layer and the current collector in lithium-ion batteries by electrochemical impedance spectroscopy. *J. Power Sources* **2019**, *409*, 139–147.
(55) Xiao, Y.; Huang, X.; Meng, J.; Zhang, Y.; Knap, V.; Stroe, D.-I. Electrochemical Impedance Spectroscopy-Based Characterization and Modeling of Lithium-Ion Batteries Based on Frequency Selection. *Batteries* **2025**, *11*, No. 11.
(56) Duan, X.; Liu, F.; Agar, E.; Jin, X. Degradation Diagnosis of $Li(Ni_{0.5}Mn_{0.2}Co_{03})O_2$/Li Half-cell by Identifying Physical Parameter Evolution Profile Using Impedance Spectra During Cycling. *J. Electrochem. Soc.* **2023**, *170*, No. 040503.
(57) Talian, S. D.; Brutti, S.; Navarra, M. A.; Moškon, J.; Gaberscek, M. Impedance spectroscopy applied to lithium battery materials: Good practices in measurements and analyses. *Energy Storage Mater.* **2024**, *69*, No. 103413.
(58) Brennan, D. A.; Mabbett, I.; Elvins, J.; Lavery, N. P.; Worsley, D. A. Mathematical framework for predicting the thermal behaviour of spectrally selective coatings within an industrial near-infrared furnace. *Eur. J. Comput. Mech.* **2016**, *25* (3), 294–308.
(59) Department for Energy Security and Net Zero. *Provisional UK greenhouse gas emissions statistics 2025, 2026* **2026** https://www.gov.uk/government/statistics/provisional-uk-greenhouse-gas-emissions-statistics-2025.
(60) Vegh, G.; Sarah, S.; Kantor, I.; Amine, K.; Srivastava, M.; Rezayi, M.; Madikere Raghunatha Reddy, A. K.; Zaghib, K. Toward Sustainable Anode Materials: LCA of Natural Graphite Processing in Québec. *Batteries* **2026**, *12*, No. 68.
(61) Rey, I.; Vallejo, C.; Santiago, G.; Iturrondobeitia, M.; Lizundia, E. Environmental Impacts of Graphite Recycling from Spent Lithium-Ion Batteries Based on Life Cycle Assessment. *ACS Sustainable Chem. Eng.* **2021**, *9* (43), 14488–14501.
(62) Natarajan, S.; Mae, T.; Teah, H. Y.; Sakurai, H.; Noda, S. Environmentally friendly regeneration of graphite from spent lithium-ion batteries for sustainable anode material reuse. *J. Mater. Chem. A* **2025**, *13* (7), 4984–4993.
(63) Gaines, L. The future of automotive lithium-ion battery recycling: Charting a sustainable course. *Sustainable Mater. Technol.* **2018**, *16*, 1–10.
(64) Badenhorst, C.; Kuzniarska-Biernacka, I.; Guedes, A.; Mousa, E.; Ramos, V.; Rollinson, G.; Ye, G.; Valentim, B. Recovery of Graphite from Spent Lithium-Ion Batteries. *Recycling* **2023**, *8*, No. 79.
(65) Liang, Z.; Cai, C.; Peng, G.; Hu, J.; Hou, H.; Liu, B.; Liang, S.; Xiao, K.; Yuan, S.; Yang, J. Hydrometallurgical recovery of spent lithium ion batteries: environmental strategies and sustainability evaluation. *ACS Sustainable Chem. Eng.* **2021**, *9* (17), 5750–5767.
(66) He, Y.; Yuan, X.; Zhang, G.; Wang, H.; Zhang, T.; Xie, W.; Li, L. A critical review of current technologies for the liberation of electrode materials from foils in the recycling process of spent lithium-ion batteries. *Sci. Total Environ.* **2022**, *766*, No. 142382.
(67) Ma, X.; Ge, P.; Wang, L.; Sun, W.; Bu, Y.; Sun, M.; Yang, Y. The recycling of spent lithium-ion batteries: crucial flotation for the separation of cathode and anode materials. *Molecules* **2023**, *28* (10), No. 4081.
(68) Harper, G. D. J. Upcycle for enhanced performance. *Nat. Sustainable* **2023**, *6* (7), 725–726.
(69) Thompson, D.; Hyde, C.; Hartley, J. M.; Abbott, A. P.; Anderson, P. A.; Harper, G. D. J. To shred or not to shred: A comparative techno-economic assessment of lithium ion battery hydrometallurgical recycling retaining value and improving circularity in LIB supply chains. *Resour. Conserv. Recycl.* **2021**, *175*, 105741.
(70) Glöser-Chahoud, S.; Huster, S.; Rosenberg, S.; Baazouzi, S.; Kiemel, S.; Singh, S.; Schneider, C.; Weeber, M.; Miehe, R.; Schultmann, F. Industrial disassembling as a key enabler of circular economy solutions for obsolete electric vehicle battery systems. *Resour. Conserv. Recycl.* **2021**, *174*, No. 105735.
(71) Harper, G. D. J.; Kendrick, E.; Anderson, P. A.; Mrozik, W.; Christensen, P.; Lambert, S.; Greenwood, D.; Das, P. K.; Ahmeid, M.; Milojevic, Z.; et al. Roadmap for a sustainable circular economy in lithium-ion and future battery technologies. *J. Phys Energy* **2023**, *5* (2), No. 021501.
(72) Ma, X.; Meng, Z.; Bellonia, M. V.; Spangenberger, J.; Harper, G.; Gratz, E.; Olivetti, E.; Arsenault, R.; Wang, Y. The evolution of lithium-ion battery recycling. *Nat. Rev. Clean Technol.* **2025**, *1* (1), 75–94.
(73) Thompson, D. L.; Hartley, J. M.; Lambert, S. M.; Shiref, M.; Harper, G. D. J.; Kendrick, E.; Anderson, P.; Ryder, K. S.; Gaines, L.; Abbott, A. P. The importance of design in lithium ion battery recycling – a critical review. *Green Chem.* **2020**, *22* (22), 7585–7603.

Downloaded from pubs.acs.org/asmcd/article-pdf/3/8/2751/6507516/rm-2026-00237h.pdf by UNIV OF BATH user on 29 October 2026

https://doi.org/10.1021/acssusresmgt.6c00237
ACS Sustain. Resour. Manag. 2026, 3, 2751–2765